Melt pool turbulence effects on the interface between dissimilar materials maufactured by directed energy deposition with laser and powder

Vincent Jacquier, Julien Zollinger, Philippe Zeller, Morgan Dal, Frédéric Schuster, Hicham Maskrot, Wilfried Pacquentin

To cite this version:

Vincent Jacquier, Julien Zollinger, Philippe Zeller, Morgan Dal, Frédéric Schuster, et al.. Melt pool turbulence effects on the interface between dissimilar materials maufactured by directed energy deposition with laser and powder. Journal of Materials Engineering and Performance, 2021, 30 (12), pp.8810-8820. 10.1007/s11665-021-06279-x . cea-03412001

HAL Id: cea-03412001

https://cea.hal.science/cea-03412001v1

Submitted on 2 Nov 2021

Melt pool turbulence effects on the interface between dissimilar materials manufactured by Directed Energy Deposition with laser and powder

Journal:	*Journal of Materials Engineering and Performance*
Manuscript ID	JMEP-21-05-24017.R1
Manuscript Type:	Technical Article
Date Submitted by the Author:	27-Jul-2021
Complete List of Authors:	JACQUIER, Vincent; CEA, Department of Physical Chemistry Zollinger, Julien; IJL Zeller, Philippe; CEA, Department of Physical Chemistry Dal, Morgan; CNAM Schuster, F; CEA, Department of Physical Chemistry Maskrot, Hicham; CEA, Department of Physical Chemistry Pacquentin, Wilfried; CEA : French Alternative Energies and Atomic Energy Commission,
Keywords:	Additive Manufacturing, Modeling and Simulation, Dissimilar Materials

Melt pool turbulence effects on the interface between dissimilar materials manufactured by Directed Energy Deposition with laser and powder

JACQUIER Vincent[1], ZOLLINGER Julien[2], ZELLER Philippe[3], DAL Morgan[4], SCHUSTER Frédéric[5], MASKROT Hicham[1], PACQUENTIN Wilfried[1]

1. Université Paris-Saclay, CEA, Service d'Etudes Analytiques et de Réactivité des Surfaces, 91191, Gif-sur-Yvette, France
2. IJL, Université de Lorraine, CNRS, 54000 Nancy, France
3. Université Paris-Saclay, CEA, Service de la Corrosion et du Comportement des Matériaux dans leur Environnement, 91191, Gif-sur-Yvette, France
4. PIMM, Arts et Metiers Institute of Technology, CNRS, CNAM, HESAM University, 75013 Paris, France
5. Cross-Cutting Program on Materials and Processes Skills, CEA, Université Paris-Saclay, 91191 Gif-sur-Yvette, France

Corresponding author email: wilfried.pacquentin@cea.fr

Directed energy deposition (DED) with laser and powder allows the manufacturing of multi-metallic near net shape structures, with control over the feedstock composition and intense liquid mixing of elements. To better understand the multi-physical aspects of the melt pool and strive towards local composition prediction, a 3D finite element model of the laser deposition of chromium on stainless steel has been developed. A modified v^2-f model is implemented to investigate the effect of melt pool turbulence on heat, momentum, and mass transport. The model is formulated in the moving frame of the laser, which allows reducing the domain size and the computation time. Overlapping on previous tracks is included by updating the upstream face boundary conditions with the composition and free-surface shape of the calculated molten cross-section. This allows for fast computation of the steady-state solution of the layer formation. Simulation results are compared to the composition analysis of a part containing an interface between chromium and stainless steel manufactured using a controlled atmosphere laser powder-DED system. The diffusive effects induced by turbulence are analyzed with regard to a laminar simulation and are found to have a significant impact on the maximum fluid velocity and temperature. Melt pool turbulence thickens the flow vortices and homogenizes the core of the melt pool, which is consistent with the experimental results. Chemical heterogeneities can be seen at the boundary with the substrate and are reviewed in light of the simulation results.

Keywords: Additive Manufacturing, DED, modeling and simulation, dissimilar materials

1. Introduction

DED (Directed Energy Deposition) is a versatile additive manufacturing process, capable of producing and repairing large metallic parts. In the last decade, numerous studies (Ref 1–4) highlighted the potential of DED for the creation of advanced multi-materials parts. Their production remains challenging (Ref 5–8) due to the differences in thermophysical properties between the different materials and the occurrence of specific defects. Numerical simulation is a powerful tool to help understand how physical phenomena affect part quality (Ref 9–11). The behavior of melt pools created by localized heating of metals has long been a subject of great interest, driven by the widespread use of welding (Ref 12) and further promoted by the rise of additive manufacturing (Ref 13). Early theoretical calculations and imaging of melt pool dynamics (Ref 14–16) revealed the presence of strong fluid motions induced by surface tension gradients. Numerical modeling of laser surface melting (Ref 17) assessed the crucial role of this flow circulation on the melt pool shape and solidification variables. Further progress in process modeling and simulation (Ref 18, 19) made it possible to track the free surface of the melt pool, quantify the effects of powder injection, and model the mixture of multiple chemical species. Modern models deliver comprehensive three-dimensional simulations including various mechanical and physical phenomena and providing satisfactory predictions of the molten zone dimensions. Transient calculations (Ref 20–22) allow the explicit simulation of the deposition of several tracks deposition by DED but require large computational resources impeding practical daily use. Furthermore, even the most comprehensive models leave out some physical phenomena. In particular, melt pool turbulence is generally neglected (Ref 17–26) or handled by the use of *ad hoc* effective properties (Ref 27–30).

A recent camera analysis of melt pool surface dynamics during laser deposition (Ref 31) reported strong fluctuations in the speed and direction of the tracked particles. The authors suggested this randomness to be caused by a turbulent melt flow regime and the impact of the powder particles on the surface. Wirth (Ref 28, 32) further compared the experimentally measured velocities and chemical distributions with the results of a laser deposition model assuming laminar flow. Calculated mean velocities were overestimated, and mixing of the melt pool with the substrate was underestimated. Effective enhancements of viscosity and thermal conductivity allowed to fit the simulation to experimental results. Wirth (Ref 28) ultimately emphasized the need for a physically-based implementation of turbulence in future models. Zhang et al. (Ref 33) analyzed the evolution of bubbles at the surface of the melt pool during DED with laser and powder. The hypothesis for the cause of the bubbles' erratic motion were the melt pool fluid turbulence and particles impingement. Turbulence studies on metal melt pool with comparable size, but without powder injection, confirmed the presence of a turbulent regime (Ref 29, 34, 35). Chakraborty et al. (Ref 36) revealed the influence of turbulence during laser alloying with a flat and wide melt pool (around 2.5 mm) by comparing the results of a laminar model with a turbulent one. In their study, the diffusive effects induced by fluid turbulence tended to homogenize species concentrations, leading to a significantly better agreement with experimental chemical analysis as compared to the laminar simulation. Temperatures and velocities in the melt pool were affected as well. The authors conclusively affirm the necessity of turbulent modeling during high-power laser surface applications.

The k-ε high Reynolds numbers is generally selected to model the turbulence effects. Recently the v^2-f low Reynolds RANS model has been used to study the casting of an aluminum alloy (Ref 37). This model was found to better account for the turbulence damping by the mushy zone (compared to a k-ε model), by taking into account the anisotropic nature of turbulence from the melt pool core to the solid-liquid boundary.

To fully master the DED manufacturing of multi-materials, it will be of great help to develop and use predictive models allowing the analysis and optimization of the process. The present model aims at providing additional insights into the complex transport phenomena at play during the creation of a layer by DED. Based on the mentioned studies, the implementation of a turbulent model seems to be necessary to better understand and quantify the effect of melt pool turbulence during DED.

The melt pool generated during additive manufacturing with DED is often smaller than 2.5 mm to allow good feature resolution. The intensity of fluid turbulence decreasing with the size of the system, there exists a melt pool width limit where turbulence will become negligible. However a definite Reynolds critical number is not currently available for our problem, hence we will use a turbulence model capable of handling low Reynolds situations.

Through an innovative way of taking into account the overlapping of the computed melt pool on the previous tracks, we achieve a fast and self-consistent steady-state solution of the layer construction. The free surface geometry is determined from the force balance equation at the gas-liquid boundary. By simulating the mixing of the feedstock inflow with the substrate, as well as the evolution of turbulence through the use of a modified v^2-f model, we analyze the influence of turbulence on the composition distribution in the solidified layer.

The model is applied to a case study of the manufacturing by DED of a chromium block on a 316L steel substrate. Chromium is used as protection against corrosion (Ref 38), and can also serve as filler material to deposit refractory alloys on steels (Ref 2, 39). Chromium melting point is around 400 K greater than the 316L liquidus temperature (Table 4), thus the deposition of the first layer is dissimilar and requires careful adjustments of parameters to produce a fully melted layer of chromium on 316L. The use of the model allows for a better understanding of the physics of this complex dissimilar deposition and an assessment of the influence of turbulence on the interface between the chromium deposit and the 316L substrate.

2. Materials and Methods

2.1. Case study experiment

2.1.1. Materials, processing systems, manufacturing

Using an OPTOMEC – LENS 500 unit, a block of chromium was additively manufactured upon a 100x50x20 mm 316L substrate in an argon chamber in which the atmosphere was recycled and filtered to keep the oxygen mass fraction below 20 ppm during the process. A coaxial nozzle allows focusing the powder jet on the surface, at a working distance of 10 mm, with argon as the carrier gas. The focused powder spot width is around 4 mm. Through a YLS-3000-CT fiber laser unit, a CW beam with a 1070 nm wavelength generates at the surface a defocused spot with a theoretical beam width of 1.4 mm. The substrate is translated horizontally by the CNC unit, programmed by G-Code, allowing additive manufacturing. The diameter of the spherical chromium powder was between 45 µm and 100 µm. The chemical compositions of the 316L substrate and the chromium powder are presented in Table 1 and Table 2, respectively.

5 layers of pure chromium (> $99\%_{wt}$) were built on the 316L substrate. The first layer consisted of 8 unidirectional tracks of 30 mm in length with a hatching distance of 0.8 mm and a layer mean thickness of 0.49 mm. The laser power was set to 800 W and the travel speed to 10 mm/s. The effective volumetric deposition rate was around 3.9 mm^3/s.

2.1.2. Post-fabrication preparation and analysis

After its manufacturing, the sample was cut in the middle length, perpendicularly to the tracks. Standard mechanical grinding and polishing were followed by optical analysis. EDS analysis was performed with a XFlash 6 | 30 Bruker detector on a TESCAN VEGA3 scanning electron microscope. Standardless quantification of a line scan was achieved with the $\Phi(\rho z)$ method and more than 10 000 counts per point.

2.2. Multiphysics modeling

2.2.1. Model objectives, reference frame, and geometry

The goal of the model is to compute the steady-state solution of the deposition of a linear track overlapping the previous ones. During the formation of a layer by the successive overlapping of linear tracks, the melt pool will gradually evolve towards an "overlapping steady-state". At this point, no significant difference will be detectable between the melt pools of the following overlapping tracks. This overlapping steady-state is of great interest because it will govern most features of a wide layer such as its dimensions, composition profile, and solidification characteristics.

The model is formulated in the frame of the laser. As illustrated in Figure 1 the fluid domain is a restricted volume encompassing the zone where the melt pool develops. Outside the fluid domain, only the temperature and surface deformation of previous tracks are computed. The surrounding gas, powder jet, and laser beam propagation are not explicitly modeled.

Figure 1 displays the geometry outlines and the orientation of the 3D Cartesian coordinate system, with the meshed fluid domain at the top center. The blue color indicates the front face of the thermal domain and the front face of the fluid domain. The red arrow denotes the central axis of the laser beam and powder stream. The black arrow designates the direction of the substrate translation.

2.2.2. Simplifying assumptions

- Fluid: the molten metal fluid is regarded as a continuous liquid mixture. The 316L substrate is considered as a pure component, therefore we use an effective diffusion coefficient for the diffusion of chromium in 316L. The influence of gravity on the melt flow is neglected with respect to the predominant Marangoni effect (Ref 32). Fluid turbulence is modeled using a modified v^2-f low Reynolds RANS formulation.
- Powder: the powder inflow at the melt pool surface is formulated as vertical, uniform, and continuous, implying instantaneous dissolution at the surface. The powder particles are assumed to have been heated by the laser up to the surface temperature. They are a source of mass and momentum at the surface. Their influence on the fluid tangential stress and turbulent variables at the surface is not accounted for in this study.

- Previous tracks: since we address the steady-state solution of overlapping tracks, it is consistent to assume that in this regime all produced tracks will be identical. Thus we use the computed shape of the current track and its concentration field to describe the previous tracks. The details of the implementation of this method are given in the boundary conditions section.
- Thermal: the temperature homogenization between two consecutive tracks is assumed to be complete. In other words, the effect of the unsteady thermal field of previous tracks on the melt pool steady-state solution is neglected. The thermal field outside the simulation domain is approximated by appropriate boundary conditions.

2.2.3. Governing equations

- Mass and momentum

The velocity and pressure fields satisfy two Navier-Stokes equations, i.e. mass conservation (Eq. 1) and linear momentum conservation (Eq. 2). To achieve the decay of the fluid motion in the mushy zone, the viscosity is gradually increased up to an artificial constant μ_S at the solidus temperature. For lower temperatures, numerical constraints are applied to the velocity field to guarantee the absence of spurious motion in the solid.

(Eq. 1) $\vec{\nabla} \cdot (\rho \vec{u}) = 0$

(Eq. 2) $\rho \vec{u} \cdot \vec{\nabla} \vec{u} = \vec{\nabla} \cdot \left((\mu + \mu_T)\left((\vec{\nabla} \vec{u}) + (\vec{\nabla} \vec{u})^{\mathrm{T}} \right) - p\mathbf{I} \right)$

- Turbulence

The Reynolds stress is modeled through the Boussinesq hypothesis. The eddy viscosity μ_T scalar field is obtained using a modified v^2-f RANS model. Whereas the k-ε models use k as the turbulent velocity scale and k/ε as the turbulent time scale, the v^2-f low Reynolds model (Ref 40,41) allows taking into account the anisotropic nature of turbulence by also computing v^2 (the velocity fluctuation normal to the streamlines), and using it as the velocity scale for turbulence. An additional variable f (the elliptic blending function) is introduced as well, as a source term for v^2, and accounts for the global effect of wall blocking. Contrary to isotropic high Reynolds RANS models which rely on local damping functions to emulate the suppression of turbulence by the walls, this effect is consistently modeled in the v^2-f low Reynolds model through the global reduction of v^2 by the walls.

The numerically robust ζ-α variant (Ref 42) is the one used in this study, which solves for the turbulent relative fluctuations $\zeta = v^2/k$ instead of v^2, and with α being f. Additional damping source terms are added in our model to gradually cancel turbulence variables in the mushy zone. The definition and value of all the model parameters can be found in Hanjalić's work (Ref 42).

(Eq. 3) $\rho \vec{u} \cdot \vec{\nabla} k = \vec{\nabla} \cdot \left(\left(\mu + \frac{\mu_T}{\sigma_k} \right) \vec{\nabla} k \right) + P_k - \rho \varepsilon + S_m k$

(Eq. 4) $\rho \vec{u} \cdot \vec{\nabla} \varepsilon = \vec{\nabla} \cdot \left(\left(\mu + \frac{\mu_T}{\sigma_\varepsilon} \right) \vec{\nabla} \varepsilon \right) + \left(\frac{C'_{\varepsilon 1}}{\tau} \right) P_k - \left(\frac{C'_{\varepsilon 2}}{\tau} \right) \rho \varepsilon + S_m \varepsilon$

(Eq. 5) $\rho \vec{u} \cdot \vec{\nabla} \zeta = \vec{\nabla} \cdot \left(\left(\mu + \frac{\mu_T}{\sigma_\zeta} \right) \vec{\nabla} \zeta \right) + \frac{2}{k} \left(\alpha^3 \mu + \frac{\mu_T}{\sigma_k} \right) \vec{\nabla} k \cdot \vec{\nabla} \zeta + (1 - \alpha^3) f_w + \alpha^3 f_h - \frac{\zeta}{k} P_k + S_m \zeta$

(Eq. 6) $L_T^2 \vec{\nabla}^2 \alpha + 1 = \alpha + S_m \alpha$

(Eq. 7) $\mu_T = \rho C_\mu k \zeta \tau$

- Thermal energy

Thermal energy conservation (Eq. 8) is used to obtain the temperature distribution, with the implementation of the apparent heat capacity to model the latent heat exchange during fusion and solidification.

(Eq. 8) $\rho \left(c + L_f \frac{d(f_L - 0.5)}{dT} \right) \vec{u} \cdot \vec{\nabla} T = - \vec{\nabla} \cdot \vec{q}$

(Eq. 9) $\vec{q} = - \left(k_{th} + c \frac{\mu_T}{Pr_T} \right) \vec{\nabla} T$

Pr_T (Eq. 9) is the turbulent Prandtl number governing the intensity of heat turbulent diffusion relative to momentum turbulent diffusion. The Kays-Crawford model is used to estimate its value (Ref 43), which in this study is found to be around 1.5 in the core of the melt pool.

- Mass transfer

The species conservation equation (Fick's law - Eq. 10) allows to compute the distribution of the mass fractions of the chromium powder and the 316L substrate:

(Eq. 10) $$\rho\vec{u}\cdot\vec{\nabla}\omega_i = -\vec{\nabla}\cdot\vec{j}_i$$

(Eq. 11) $$\vec{j}_i = -\left(\rho D_m + \frac{\mu_T}{Sc_T}\right)\left(\vec{\nabla}\omega_i - \omega_i\textstyle\sum_k\vec{\nabla}\omega_k\right)$$

The last term of the flux expression (Eq. 11) is the mixture diffusion correction, which enforces the net diffuse mass flux to be zero. Sc_T (Eq. 11) is the turbulent Schmidt number, governing the intensity of the mass turbulent diffusion relatively to the momentum turbulent diffusion. The Kays-Crawford model is used to estimate its value (Ref 43) which in this study is found to be around 0.85 in the core of the melt pool.

- Free surface

The steady-state of the free surface deformation minimizes the total surface energy which depends on surface tension, gravity, external pressure, fluid pressure, and normal viscous stress (Ref 17). A dimensional analysis performed by Gan (Ref 23) revealed that surface tension was the dominant force during DED. Therefore in this study we only retain surface tension. The equation (Eq. 12) is solved in the deformed geometry frame.

(Eq. 12) $$-\vec{\nabla}_g\cdot\left(\frac{\gamma}{\sqrt{1+\left(\frac{\partial\phi}{\partial X_g}\right)^2+\left(\frac{\partial\phi}{\partial Y_g}\right)^2}}\vec{\nabla}_g\phi\right) = \lambda_\phi$$

(Eq. 13) $$\left(\int_{L_{gx_{rear}}}\phi\, dL_g - \int_{L_{gx_{front}}}\phi\, dL_g\right)U_0 = HD\ LT\ U_0$$

λ_ϕ is a Lagrange multiplayer ensuring fulfillment of the volumetric deposition rate constraint (Eq. 13).

The right term corresponds to the experimental volumetric deposition rate. In this study, the exact experimental powder distribution being unknown, we use the experimental hatching distance and layer thickness as input variables to estimate the volumetric deposition rate (Eq. 13). The surface elevation ϕ is thereafter applied at the top surface through the ALE method (Arbitrary Lagrangian Eulerian method). With this method, the nodes of the domain mesh are displaced (Lagrangian) and a correction is added to the fluid to allow an Eulerian calculation.

2.2.4. Source and boundary terms

- Mass and momentum

On the front face fluid is entering with velocity equal to -10 mm/s in the direction of deposition. At the rear face a zero pressure gradient condition is applied. On the top face, the addition of mass from the chromium powder, and the tangential stress generated by the surface tension variations with temperature and mass fraction write:

(Eq. 14) $$-\vec{u}\cdot\vec{n} = \frac{\vec{j}_{Cr_P}}{\rho}\cdot\vec{n}$$

(Eq. 15) $$\overrightarrow{\sigma_t} = f_L\vec{\nabla}_t\gamma$$

- Turbulence

The source terms S_m included in the turbulence equations allow for the gradual cancellation of the variables in the mushy zone:

(Eq. 16) $$S_m = -\left(\frac{10^{10}(1-f_L)^2}{f_L^3+0.01}\right)$$

No physical background is available to estimate the form and magnitude of those terms. The parameter values were therefore iteratively adjusted to ensure that the corresponding variables in the solid zone go down to zero while maintaining numerical stability. A zero normal gradient condition is imposed on all faces for all turbulence variables.

- Thermal energy

The front, rear, and side faces are thermally insulated. On the bottom face we impose a constant temperature of 100°C. Comparing this configuration with a 50 times larger geometry with ambient temperature conditions on the side and bottom faces the maximum temperature change remains below

1%. We therefore use this reduced geometry as an approximation of an infinite geometry. The top face is heated by the laser:

(Eq. 17) $$-\vec{q}\cdot\vec{n}=\left(\frac{\alpha_l P_0}{2\pi\left(\frac{\varnothing_l}{4}\right)^2}exp\left(-\frac{x^2+y^2}{2\left(\frac{\varnothing_l}{4}\right)^2}\right)\overrightarrow{e_3}\right)\cdot\vec{n}$$

- Mass transfer

On the front face, the calculated concentration field of the solidified melt pool is used to emulate the previous tracks. The inflow concentration field at the front face is therefore equal to the rear face outflow concentration field translated through the hatching distance:

(Eq. 18) $$\omega_i=\omega_i(x_{rear},y-HD,z)$$

A zero flux condition is used for the bottom, rear, and side faces. On the top face, the addition of mass from the chromium powder:

(Eq. 19) $$-\vec{j}_{316L}\cdot\vec{n}=0$$

(Eq. 20) $$-\vec{j}_{Cr}\cdot\vec{n}=\left(\vec{j}_{Cr_P}\cdot\vec{n}\right)(1-\omega_{Cr})$$

(Eq. 21) $$\vec{j}_{Cr_P}=\frac{f_L\,(HD\;LT\;U_0)\rho_{CrS}}{\int_{S_{top}}(f_L\,n_z)dS}\vec{e}_3$$

- Free surface

A zero contact angle is imposed behind the solidification front of the melt pool surface. The front edge shape is equivalent to the rear edge shape translated by the hatching distance, hence we apply the following condition at the front of the melt pool surface:

(Eq. 22) $$\phi=\phi(x_{rear},y-HD,z)$$

2.2.5. Material properties

The properties of chromium and 316L stainless steel, selected from the literature, are listed in Table 4. The solid and liquid properties are approximated by their value close to the solidus and liquidus temperature respectively. Linear rules of mixture are applied to approximate the mixture and mushy zone properties.

The value of D_{m_L} was estimated from the diffusion of chromium in molten iron (Ref 44). The value of D_{m_S} corresponds to an artificial solid diffusion used to improve numerical stability. The solidus temperature T_S was artificially set to 100K below the mixture liquidus temperature, for the mushy zone to be sufficiently resolved by the mesh. The artificial solid surface tension γ_S and solid viscosity μ_S were presented in the previous section. The evolution with temperature of the liquid chromium viscosity μ_{Cr} is plotted in Figure 2.

2.2.6. Numerical realization

The mathematical problem is numerically solved using the finite element method within the COMSOL Multiphysics® software package. All variables are discretized with linear shape functions. Streamline and crosswind diffusions are used to stabilize the transport equations. The liquid domain is discretized using a structured quadrilateral mesh with a minimal size of 20 μm, which was found to be a reasonable compromise between solution accuracy and computational time. The solid domain is discretized using an unstructured tetrahedral mesh. Each variable is scaled by its maximum values. Each set of governing equations is successively solved by the PARDISO direct linear solver (Ref 45). The iteration process is conducted until the relative difference with the previous solution drops below 10^{-3}. The total number of degrees of freedom solved for the turbulent model is around 2.2 million. A laptop workstation with 8 CPU cores clocked at 2.4 GHz reaches the turbulent model solution in around 7 hours. Although the v^2-f model introduces four additional variables, the computational effort remains manageable thanks to the choice of solving the equations in the moving frame of the laser, thus requiring fewer mesh elements and allowing the use of a stationary study. Indeed CPU time is of the same order as transient calculations of several tracks deposition without the fluid movements and species diffusion (Ref 46). The laminar model contains 36% fewer degrees of freedom, but more convergence steps are required to achieve convergence because of the higher velocity gradients and of the turbulent nature of the system. The solution is attained in around 5 hours.

3. Results and discussion

3.1. Simulations

Figure 3 displays the turbulent model solution in the liquid domain, with the melt pool developed at its center and overlapping the previous track. The composition of the previous track can be seen at the front face of the fluid domain. An outward flow pattern occurs at the melt pool surface, as excepted when the liquid surface tension decreases with temperature. The turbulent and laminar solutions exhibit similar melt pool dimensions, with a width of around 1.25 mm for both models.

The Reynolds number (Table 5) is calculated as:

$$\text{(Eq. 23)} \qquad \mathcal{Re} = \frac{U^{max}_{melt\ surface}}{\nu^{max}_{melt\ surface}} \frac{Length_{pool}}{2}$$

As seen in Table 5, compared to the laminar model, the turbulent case undergoes a lowering of the peak temperature and velocity at the melt pool surface. These reductions prove that melt pool turbulence is activated enough to affect the melt pool.

The averaged turbulence scheme models a part of the advective transport as diffusive transport, by adding a turbulent diffusion quantity to the diffusion term (Eq. 2, 9, 11). This enhancement of diffusion is only a modeling point of view that accounts for the local advective transport caused by the turbulent eddies formed in the real turbulent fluid, transported by diffusion and advection and ultimately damped by the fluid viscosity or by the walls. The calculation indicates (Table 6) that this turbulent diffusion enhances momentum diffusivity up to a factor of 20 (compared to the liquid intrinsic kinematic viscosity) and thermal diffusivity up to a factor of 0.6 (compared to the liquid intrinsic thermal diffusivity).

High velocities are generated at the surface by the thermal gradients and result in the creation of vortices in the melt pool revealed by the flow streamlines in Figure 4. Because a higher viscosity generally tends to spread out the vorticity the additional momentum diffusivity accounting for turbulence widens the melt pool vortices (Figure 4).

In both models about 0.1 mm of the 316L substrate is melted and partially mixed with the chromium-rich melt pool (Figure 4). The irregular shape of the liquidus isotherm reveals the complex relationship between fluid flow and composition distribution. The chromium melting temperature being around 400 K above the 316L liquidus, an anomalously jagged solidification front is formed at the boundary between the melt pool and the substrate.

Figure 5 displays the chromium mass fraction distribution in the (y,z) cross-section of the solidified last track overlapping the previous - emulated – one (on the right). Figure 10 reveals the chromium composition profile along the dashed arrows. A homogeneous zone exists at the top of the tracks, about 200 µm thick in the case of the turbulent model (horizontal part of the red curve in Figure 10), and about 100 µm thick for the laminar model. The larger homogeneous zone in the turbulent model surely results from the thicker rear vortex together with the enhancement of effective mass diffusivity up to a factor of 7000 (Table 6). In the laminar model, species mixing is essentially caused by advective transport, in such a way that the final concentration distribution in the layer is controlled by the complex flow circulation in the melt pool. In the turbulent case the larger vortices, enhanced local mixing, and reduction of the fluid velocity shift the species mixing mechanism from advection-dominated to a more diffusion-controlled process, which tends to smooth out the mass fraction iso-contours (Figure 5).

Figure 6 displays the cross-length distribution of the turbulent kinematic viscosity, which relates to the strength of the local momentum diffusion accounting for the effect of turbulent eddies. It reveals that the most turbulent areas of the melt pool flow are near the surface, generated by the strong velocity gradients induced by the Marangoni shear stress.

Examination of the ζ and α evolution through the melt pool leads to a better understanding of the non-local and anisotropic effect of the solid boundaries on turbulence. A value of α lower than one indicates that turbulence is damped because fluid motion is hindered by the melt pool boundaries. From Figure 7 we can conclude that turbulence in the melt pool is globally affected by the presence of the melt pool boundaries, up to the free surface. The value of ζ is also less than one, which denotes that the turbulent flow is anisotropic throughout the melt pool. This anisotropy is the consequence of the global damping effect of the melt pool boundaries, as well as the strong rotational nature of the flow in the melt pool. These observations highlight the relevance of the v^2-f model to describe the turbulent flow in a melt pool subjected to Marangoni effects. Indeed a k-ε model considers the wall blocking effect only at the local scale, i.e. close to the liquid-solid boundary, and assumes isotropic turbulence (ζ equals to 1). This would result in an overestimation of the eddy viscosity (Ref 37).

To further clarify the importance of fluid turbulence on the melt pool, we performed additional simulations with different melt pool widths (between 0.04 mm and 8 mm). The laser spot size, power, and feed rate are adjusted to produce melt pools with the same ratio of width to laser spot size and height to laser spot size as in the previously described simulation of Figure 5. Figure 8 presents the maximum value of the ratio of turbulent viscosity ν_T to maximum intrinsic viscosity ν_0, for different Reynolds numbers Re* (Eq. 23). For a better analysis of the turbulence effect, the characteristic velocity used to calculate the Reynolds number Re* was chosen to be the velocity at maximum surface turbulent viscosity ν_T. As expected, wider melt pools result in higher Re* and thus stronger fluid turbulence, which enhances the differences between laminar and turbulent simulations regarding temperatures, velocities, and mixing of elements. The maximum turbulent viscosity becomes almost equal to the maximum intrinsic viscosity when Re* is equal to 92, corresponding to a melt pool width of 0.04 mm. An inflection point is discernible at some Re* value between 268 and 446. This correlates to the range where the calculated average turbulent viscosity in the melt pool exceeds the maximum intrinsic viscosity. It corresponds respectively to melt pool widths between 0.42 mm and 4.2 mm. It should be noted that calculations with the laminar model and melt pools wider that 1.25 mm did not reach convergence and may require the use of much smaller mesh sizes and a transient calculation with quite small step sizes. This analysis suggests that fluid turbulence is fully activated when Re* is greater than ~450 (width of 4 mm), and on the other hand could be neglected when Re* is smaller than ~100 (width of 0.04 mm). Hence in the 1.25 mm wide melt pool case described above (Figures 3 to 7) resulting in a Re* of 330 turbulence is not negligible but may also not be fully activated. The use of the low Reynolds RANS model instead of a high Reynolds model appears necessary to correctly describe fluid turbulence in a melt pool close to 1 mm in width.

3.2. Experimental analysis

Figure 9 displays the experimental cross-section of the last track of the first layer, with the surface and solidified zone shapes outlined. The track core appears homogenous, which is confirmed by the examination of the EDX composition measurements (Figure 10). Unmixed areas can be seen at the boundary between the chromium layer and the 316L substrate. Macrosegregation often occurs during fusion processing of dissimilar metals and has been extensively characterized by welding studies (Ref 47, 48). The fusion temperature of chromium being greater than the liquidus temperature of 316L, there exist areas at the melt pool-substrate interface where the chromium-rich melt pool will tend to solidify while the substrate remains in liquid phase. This results in a large and unstable solidification front (as seen with the simulation in Figure 4), generating layered unmixed zones located near the boundary between the chromium layer and 316L substrate. Undissolved chromium particles are also detected at this boundary. We attribute their presence to the use of a wide powder jet, injecting powder particles into melt pool peripheral areas where the simulation indicates the presence of liquid cooler than the chromium melting point (Figure 3). Those particles still undergo dissolution in the undersaturated liquid to some extent and may even be reintegrated by convection in hotter inner layers of the melt pool. However, the short solidification times of the process apparently prevents the full dissolution of some particles.

3.3. Comparisons and discussion

The relative deviation between the calculated and experimental average chromium mass fractions in the chromium layer (Figure 10) amounts to 10% for the laminar solution, whereas the turbulence solution deviation is only 5%. As for the boundary zone, it seems clear that chromium penetration in the substrate is over-estimated by the models. However, Figure 9 indicates that the shape of the experimental substrate molten zone is close to the simulated one. The substrate appears to have been melted to a depth close to the simulation prediction, but its mixing with the chromium-rich melt pool core was weaker than what is calculated.

During the experiment undissolved chromium powder particles in the melt pool likely disturbed the fluid flow, thereby altering the penetration of chromium into the molten substrate. Dealing with this phenomenon would be necessary to accurately predict the layer composition and amount of undissolved particles after solidification. Moreover, instead of an effective mushy viscosity, better modeling of the solidification would be necessary, including microsegregation at the solidification front and the germination and motion of grains formed in the mushy zone. Additionally, evaporation at the melt pool surface should be accounted for in case of high maximum surface temperatures. To develop a more predictive model, more accurate material properties and an experimentally calibrated powder jet inflow will also be necessary.

Overall, regarding the choice of the formulation to model the fluid dynamics of the DED process, this study has shown the non-negligible presence of turbulence. Compared to the laminar model the averaged turbulence-induced increase in diffusion reduces the gradients in temperature, velocity, and mass concentration. This affects melt flow circulation, surface temperatures, and concentration distribution in solidified tracks. Accounting for turbulence with a low Reynolds turbulence model will be necessary to properly understand and predict evaporation of volatile elements, melt pool solidification, as well as the complex composition distributions found in multi-materials parts.

4. Conclusion

The present study aimed at unraveling some complex couplings of various transport phenomena arising during DED manufacturing with dissimilar metals, based on comparisons between finite-element simulations and experiments. We showed that our innovative formulation of the problem efficiently provides the steady-state solution of a sequence of overlapping linear tracks in terms of surface shape and bulk mass fraction distributions. Melt pool fluid turbulence was modeled using a modified v^2-f low Reynolds model accounting for the globally anisotropic nature of turbulence. In our case, calculations reveal that turbulence should not be neglected when the Re* number is lower than ~100 and that the transition to a fully turbulent state takes place between Re* of ~270 and ~450. Momentum, heat, and mass transport are affected by the enhanced mixing effect induced by turbulence, especially in the core of the melt pool. Compared to a laminar model the maximum velocity and temperature are reduced and species distribution in the solidified tracks becomes more homogenous and closer to the experimentally measured profile. Overall, the study motivates further implementations of the melt pool turbulent effects without the use of *ad hoc* parameters. Using a steady-state approach for the study of melt pools produced by DED allows for more efficient simulations, which will be capable of guiding the optimization of multi-materials fabrications.

5. Acknowledgments

The authors gratefully acknowledge the technical and financial support provided by the CEA Cross-Cutting Program, as well as the CEA Cross-cutting basic research Program.

6. References

1. C. Schneider-Maunoury, L. Weiss, O. Perroud, D. Joguet, D. Boisselier, and P. Laheurte, An Application of Differential Injection to Fabricate Functionally Graded Ti-Nb Alloys Using DED-CLAD® Process, *J. Mater. Process. Technol.*, 2019, **268**, p 171–180.
2. W. Li, F. Liou, J. Newkirk, K.M.B. Taminger, and W.J. Seufzer, Investigation on Ti6Al4V-V-Cr-Fe-SS316 Multi-Layers Metallic Structure Fabricated by Laser 3D Printing, *Sci. Rep.*, 2017, **7**(1), http://www.nature.com/articles/s41598-017-08580-z. Accessed 17 December 2020.
3. C. Li, S. Ma, X. Liu, J. Li, and G. Le, Microstructures and Properties of 80W-20Fe Alloys Prepared Using Laser Melting Deposition Process, *Int. J. Refract. Met. Hard Mater.*, 2018, **77**, p 113–119, doi:10.1016/j.ijrmhm.2018.08.005.
4. D.C. Hofmann, S. Roberts, R. Otis, J. Kolodziejska, R.P. Dillon, J. Suh, A.A. Shapiro, Z.-K. Liu, and J.-P. Borgonia, Developing Gradient Metal Alloys through Radial Deposition Additive Manufacturing, *Sci. Rep.*, 2015, **4**(1), doi:10.1038/srep05357.
5. W. Meng, W. Zhang, W. Zhang, X. Yin, L. Guo, and B. Cui, Additive Fabrication of 316L/Inconel625/Ti6Al4V Functionally Graded Materials by Laser Synchronous Preheating, *Int. J. Adv. Manuf. Technol.*, 2019, **104**(5–8), p 2525–2538, doi:10.1007/s00170-019-04061-x.

6. A. Reichardt, R.P. Dillon, J.P. Borgonia, A.A. Shapiro, B.W. McEnerney, T. Momose, and P. Hosemann, Development and Characterization of Ti-6Al-4V to 304L Stainless Steel Gradient Components Fabricated with Laser Deposition Additive Manufacturing, *Mater. Des.*, 2016, **104**, p 404–413, doi:10.1016/j.matdes.2016.05.016.
7. H. Dobbelstein, E.L. Gurevich, E.P. George, A. Ostendorf, and G. Laplanche, Laser Metal Deposition of Compositionally Graded TiZrNbTa Refractory High-Entropy Alloys Using Elemental Powder Blends, *Addit. Manuf.*, 2019, **25**, p 252–262, doi:10.1016/j.addma.2018.10.042.
8. N. Chen, H.A. Khan, Z. Wan, J. Lippert, H. Sun, S.-L. Shang, Z.-K. Liu, and J. Li, Microstructural Characteristics and Crack Formation in Additively Manufactured Bimetal Material of 316L Stainless Steel and Inconel 625, *Addit. Manuf.*, 2020, **32**, p 101037, doi:10.1016/j.addma.2020.101037.
9. L. Li, X. Zhang, W. Cui, F. Liou, W. Deng, and W. Li, Temperature and Residual Stress Distribution of FGM Parts by DED Process: Modeling and Experimental Validation, *Int. J. Adv. Manuf. Technol.*, 2020, **109**(1), p 451–462, doi:10.1007/s00170-020-05673-4.
10. Z. Gan, G. Yu, X. He, and S. Li, Numerical Simulation of Thermal Behavior and Multicomponent Mass Transfer in Direct Laser Deposition of Co-Base Alloy on Steel, *Int. J. Heat Mass Transf.*, 2017, **104**, p 28–38, doi:10.1016/j.ijheatmasstransfer.2016.08.049.
11. H.L. Wei, J. Mazumder, and T. DebRoy, Evolution of Solidification Texture during Additive Manufacturing, *Sci. Rep.*, 2015, **5**(1), doi:10.1038/srep16446.
12. V. Dhinakaran, M. Varsha Shree, T. Jagadeesha, P.M. Bupathi Ram, T. Sathish, and B. Stalin, A Review on the Recent Developments in Modeling Heat and Material Transfer Characteristics during Welding, *Mater. Today Proc.*, 2020, **21**, p 908–911, doi:10.1016/j.matpr.2019.08.079.
13. H.L. Wei, T. Mukherjee, W. Zhang, J.S. Zuback, G.L. Knapp, A. De, and T. DebRoy, Mechanistic Models for Additive Manufacturing of Metallic Components, *Prog. Mater. Sci.*, 2021, **116**, p 100703, doi:10.1016/j.pmatsci.2020.100703.
14. T. Chande and J. Mazumder, Mass Transport in Laser Surface Alloying: Iron-nickel System, *Appl. Phys. Lett.*, 1982, **41**(1), p 42–43, doi:10.1063/1.93315.
15. H.C. R and R.J. R, Mechanism for Minor Element Effect on GTA Fusion Zone Geometry, *Weld. J.*, 1982, **61**(4), p 97–102, https://jglobal.jst.go.jp/en/detail?JGLOBAL_ID=200902076065662823. Accessed 13 January 2021.
16. G. Caillibotte, D. Kechemair, and L. Sabatier, “Velocity Measurements in Molten Pools during High-Power Laser Interaction with Metals,” International Society for Optics and Photonics, 1991, p 209–211, doi:10.1117/12.43652.
17. S. Kou and Y.H. Wang, Three-Dimensional Convection in Laser Melted Pools, *Metall. Trans. A*, 1986, **17**(12), p 2265–2270, doi:10.1007/BF02645924.
18. H. Qi, H. Ki, and J. Mazumder, Numerical Simulation of Multi-Material Laser Cladding by Coaxial Powder Injection, *Int. Congr. Appl. Lasers Electro-Opt.*, 2004, **2004**(1), p 607, doi:10.2351/1.5060286.
19. M. Picasso and A.F.A. Hoadley, Finite Element Simulation of Laser Surface Treatments Including Convection in the Melt Pool, *Int. J. Numer. Methods Heat Fluid Flow*, 1994, **4**(1), p 61–83, doi:10.1108/EUM0000000004031.
20. J.S. Zuback, G.L. Knapp, T.A. Palmer, and T. DebRoy, Deposit Geometry and Oxygen Concentration Spatial Variations due to Composition Change in Printed Functionally Graded Components, *Int. J. Heat Mass Transf.*, 2021, **164**, p 120526, doi:10.1016/j.ijheatmasstransfer.2020.120526.
21. H.L. Wei, F.Q. Liu, W.H. Liao, and T.T. Liu, Prediction of Spatiotemporal Variations of Deposit Profiles and Inter-Track Voids during Laser Directed Energy Deposition, *Addit. Manuf.*, 2020, **34**, p 101219, doi:10.1016/j.addma.2020.101219.
22. S. Liu, K.-M. Hong, C. Katinas, and Y.C. Shin, Multiphysics Modeling of Phase Transformation and Microhardness Evolution in Laser Direct Deposited Ti6Al4V, *J. Manuf. Process.*, 2019, **45**, p 579–587, doi:10.1016/j.jmapro.2019.07.027.
23. C. Li, Z. Yu, J. Gao, J. Zhao, and X. Han, Numerical Simulation and Experimental Study of Cladding Fe60 on an ASTM 1045 Substrate by Laser Cladding, *Surf. Coat. Technol.*, 2019, **357**, p 965–977, doi:10.1016/j.surfcoat.2018.10.099.
24. Z. Gan, G. Yu, X. He, and S. Li, Surface-Active Element Transport and Its Effect on Liquid Metal Flow in Laser-Assisted Additive Manufacturing, *Int. Commun. Heat Mass Transf.*, 2017, **86**, p 206–214, doi:10.1016/j.icheatmasstransfer.2017.06.007.
25. Z. Gan, H. Liu, S. Li, X. He, and G. Yu, Modeling of Thermal Behavior and Mass Transport in Multi-Layer Laser Additive Manufacturing of Ni-Based Alloy on Cast Iron, *Int. J. Heat Mass Transf.*, 2017, **111**, p 709–722, doi:10.1016/j.ijheatmasstransfer.2017.04.055.
26. C. Katinas, S. Liu, and Y.C. Shin, Self-Sufficient Modeling of Single Track Deposition of Ti–6Al–4V With the Prediction of Capture Efficiency, *J. Manuf. Sci. Eng.*, 2019, **141**(1), doi:10.1115/1.4041423.
27. J. Zhao, G. Wang, X. Wang, S. Luo, L. Wang, and Y. Rong, Multicomponent Multiphase Modeling of Dissimilar Laser Cladding Process with High-Speed Steel on Medium Carbon Steel, *Int. J. Heat Mass Transf.*, 2020, **148**, p 118990, doi:10.1016/j.ijheatmasstransfer.2019.118990.
28. F. Wirth, “Process Understanding, Modeling and Predictive Simulation of Laser Cladding,” ETH Zurich, 2018, https://www.research-collection.ethz.ch/handle/20.500.11850/314396. Accessed 13 January 2021.
29. A. Ebrahimi, C.R. Kleijn, and I.M. Richardson, Numerical Study of Molten Metal Melt Pool Behaviour during Conduction-Mode Laser Spot Melting, *J. Phys. Appl. Phys.*, 2020, **54**(10), p 105304, doi:10.1088/1361-6463/abca62.
30. G.L. Knapp, T. Mukherjee, J.S. Zuback, H.L. Wei, T.A. Palmer, A. De, and T. DebRoy, Building Blocks for a Digital Twin of Additive Manufacturing, *Acta Mater.*, 2017, **135**, p 390–399, doi:10.1016/j.actamat.2017.06.039.
31. F. Wirth, S. Arpagaus, and K. Wegener, Analysis of Melt Pool Dynamics in Laser Cladding and Direct Metal Deposition by Automated High-Speed Camera Image Evaluation, *Addit. Manuf.*, 2018, **21**, p 369–382, doi:10.1016/j.addma.2018.03.025.
32. F. Wirth and K. Wegener, A Physical Modeling and Predictive Simulation of the Laser Cladding Process, *Addit. Manuf.*, 2018, **22**, p 307–319, doi:10.1016/j.addma.2018.05.017.

33. P. Zhang, X. Zhou, X. Cheng, H. Sun, H. Ma, and Y. Li, Elucidation of Bubble Evolution and Defect Formation in Directed Energy Deposition Based on Direct Observation, *Addit. Manuf.*, 2020, **32**, p 101026, doi:10.1016/j.addma.2019.101026.
34. D. Chatterjee and S. Chakraborty, Large-Eddy Simulation of Laser-Induced Surface-Tension-Driven Flow, *Metall. Mater. Trans. B*, 2005, **36**(6), p 743–754, doi:10.1007/s11663-005-0078-0.
35. N. Chakraborty and S. Chakraborty, Modelling of Turbulent Molten Pool Convection in Laser Welding of a Copper–nickel Dissimilar Couple, *Int. J. Heat Mass Transf.*, 2007, **50**(9–10), p 1805–1822, doi:10.1016/j.ijheatmasstransfer.2006.10.030.
36. N. Chakraborty, D. Chatterjee, and S. Chakraborty, Modeling of Turbulent Transport in Laser Surface Alloying, *Numer. Heat Transf. Part Appl.*, 2004, **46**(10), p 1009–1032, doi:10.1080/10407780490517629.
37. G.C. Nzebuka, M.A. Waheed, S.I. Kuye, and B.I. Olajuwon, Accounting for Melt Flow Pattern and Solid Fraction Evolution in DC Casting of Al-Cu Alloy Using v^2 - F Turbulence Model, *Metall. Mater. Trans. B*, 2019, **50**(2), p 866–880, doi:10.1007/s11663-018-01502-y.
38. H.-G. Kim, I.-H. Kim, Y.-I. Jung, D.-J. Park, J.-Y. Park, and Y.-H. Koo, Adhesion Property and High-Temperature Oxidation Behavior of Cr-Coated Zircaloy-4 Cladding Tube Prepared by 3D Laser Coating, *J. Nucl. Mater.*, 2015, **465**, p 531–539, doi:10.1016/j.jnucmat.2015.06.030.
39. Molybdenum-on-Chromium Dual Coating on Steel, *Surf. Coat. Technol.*, 2009, **203**(9), p 1281–1287, doi:10.1016/j.surfcoat.2008.10.029.
40. P.A. Durbin, Near-Wall Turbulence Closure Modeling without “damping Functions,” *Theor. Comput. Fluid Dyn.*, 1991, **3**(1), p 1–13, doi:10.1007/BF00271513.
41. P.A. Durbin, Application of a near-Wall Turbulence Model to Boundary Layers and Heat Transfer, *Int. J. Heat Fluid Flow*, 1993, **14**(4), p 316–323, doi:10.1016/0142-727X(93)90004-7.
42. K. Hanjalić, M. Popovac, and M. Hadžiabdić, A Robust near-Wall Elliptic-Relaxation Eddy-Viscosity Turbulence Model for CFD, *Int. J. Heat Fluid Flow*, 2004, **25**(6), p 1047–1051, doi:10.1016/j.ijheatfluidflow.2004.07.005.
43. W.M. Kays, Turbulent Prandtl Number—Where Are We?, *J. Heat Transf.*, 1994, **116**(2), p 284–295, doi:10.1115/1.2911398.
44. “Diffusion of Chromium, Manganese and Nickel in Molten Iron Saturated with Carbon,” n.d.
45. C. Alappat, A. Basermann, A.R. Bishop, H. Fehske, G. Hager, O. Schenk, J. Thies, and G. Wellein, A Recursive Algebraic Coloring Technique for Hardware-Efficient Symmetric Sparse Matrix-Vector Multiplication, *ACM Trans. Parallel Comput.*, 2020, **7**(3), p 1–37.
46. P. Peyre, M. Dal, S. Pouzet, and O. Castelnau, Simplified Numerical Model for the Laser Metal Deposition Additive Manufacturing Process, *J. Laser Appl.*, 2017, **29**(2), p 22304, doi:10.2351/1.4983251.
47. Y.K. Yang and S. Kou, Macrosegregation Mechanisms in Arc Welds Made with Dissimilar Filler Metals, *Sci. Technol. Weld. Join.*, 2010, **15**(1), p 15–30, doi:10.1179/136217109X456979.
48. G. Liu, S. Yang, J. Ding, W. Han, L. Zhou, M. Zhang, S. Zhou, R.D.K. Misra, F. Wan, and C. Shang, Formation and Evolution of Layered Structure in Dissimilar Welded Joints between Ferritic-Martensitic Steel and 316L Stainless Steel with Fillers, *J. Mater. Sci. Technol.*, 2019, **35**(11), p 2665–2681, doi:10.1016/j.jmst.2019.05.047.
49. D.U. Furrer and S.L. Semiatin, Eds., Thermophysical Properties, *Metals Process Simulation*, ASM International, 2010, p 18–32.
50. K.C. Mills, “Recommended Values of Thermophysical Properties for Selected Commercial Alloys,” (Cambridge), Woodhead, 2002.
51. T. Yagi, Y. Ono, and M. Ushijima, Diffusion of Chromium, Manganese and Nickel in Molten Iron Saturated with Carbon, *Tetsu--Hagane*, 1970, **56**(13), p 1640–1645, doi:10.2355/tetsutohagane1955.56.13_1640.
52. P. Lacombe, B. Baroux, G. Béranger, L. Colombier, and J. Hochmann, “Les aciers inoxydables,” (Les Ulis, France), Les Editions de Physique, 1990.
53. S.V. Stankus, Density of vanadium and chromium at high temperatures, *Teplofiz. Vysok. Temp.*, 1993, **31**(4), p 565–568, http://inis.iaea.org/Search/search.aspx?orig_q=RN:25051417. Accessed 18 December 2020.
54. E.A. Brandes, G.B. Brook, and C.J. Smithells, Eds., “Smithells Metals Reference Book,” 7th ed / edited by E.A. Brandes and G.B. Brook, (Oxford ; Boston), Butterworth-Heinemann, 1998.
55. D. Hipp, A. Mahrle, and E. Beyer, Energy Coupling of Laser Radiation on AISI 304 Stainless Steel: Effect of High Temperatures and Surface Oxidation, *Materials*, 2019, **12**(17), doi:10.3390/ma12172802.
56. P. Sahoo, T. Debroy, and M.J. McNallan, Surface Tension of Binary Metal—surface Active Solute Systems under Conditions Relevant to Welding Metallurgy, *Metall. Trans. B*, 1988, **19**(3), p 483–491, doi:10.1007/BF02657748.
57. L. Battezzati and A.L. Greer, The Viscosity of Liquid Metals and Alloys, *Acta Metall.*, 1989, **37**(7), p 1791–1802, doi:10.1016/0001-6160(89)90064-3.

7. Tables

Table 1. Nomenclature.

c	heat capacity	U	velocity magnitude
c_{L_f}	apparent heat capacity	U_0	substrate travel velocity
D_m	mass diffusivity	w_{pool}	melt pool width
$\vec{e}_1, \vec{e}_2, \vec{e}_3$	global unit vectors	x, y, z	global coordinates
$\vec{e}_{g1}, \vec{e}_{g2}, \vec{e}_{g3}$	local unit vectors in deformed geometry frame	X_g, Y_g, Z_g	local coordinates in deformed geometry frame
f_L	liquid mass fraction	α	elliptic blending function
HD	hatching distance	α_l	absorptivity of the liquid at 1 µm
$\vec{j}_i$	mass flux of *i* (Cr, 316L)	ε	turbulent dissipation rate
k	turbulent kinetic energy	γ	liquid-gas surface tension
k_{th}	thermal conductivity	ζ	turbulent relative fluctuations
L_f	latent heat of fusion	$\mu,\ \nu$	dynamic and kinematic viscosity
LT	layer thickness	ρ	density
$\vec{n},\ \vec{t}$	normal and tangential vector	σ_t	tangential stress
p	pressure field	ω_i	mass fraction of *i* (Cr, 316L)
$\vec{q}$	heat flux	ϕ	surface elevation
T	temperature field	$\varnothing_l$	D4σ width of the laser beam at the surface
T_0	ambient temperature	$\vec{\nabla}$	gradient operator
T_b	substrate bottom temperature	$\vec{\nabla}_g$	gradient operator in deformed geometry frame
$T_L,\ T_S$	liquidus and solidus temperatures	$\vec{\nabla}_t$	tangential gradient operator
$\vec{u}$	velocity vector field		

Table 2. Chemical composition of the 316L substrate, in wt%.

	C	Cr	Fe	Mn	Mo	N	Ni	O	S	Si
316L	0.015	17.2	69.1	1.21	2.33	0.073	9.65	0.0045	0.022	0.39

Table 3. Chemical composition of the chromium powder, in wt%.

	Al	C	Cr	Fe	N	O	Si
Cr powder	0.0020	0.0022	99.7	0.12	0.0058	0.10	0.030

Table 4. Material properties.

Symbol	Unit	Cr powder	Ref	316L	Ref
c_L	$J\,kg^{-1}\,K^{-1}$	780	(Ref 49)	800	(Ref 50)
c_S	$J\,kg^{-1}\,K^{-1}$	1085	(Ref 49)	730	(Ref 50)
D_{m_L}	$m^2\,s^{-1}$	$3 \cdot 10^{-9}$	(Ref 51)	$3 \cdot 10^{-9}$	(Ref 51)
D_{m_S}	$m^2\,s^{-1}$	$1 \cdot 10^{-11}$		$1 \cdot 10^{-11}$	
k_{th_L}	$W\,m^{-1}\,K^{-1}$	35	(Ref 49)	28	(Ref 50)
k_{th_S}	$W\,m^{-1}\,K^{-1}$	45	(Ref 49)	32	(Ref 50)
L_f	$J\,kg^{-1}$	$4.0 \cdot 10^5$	(Ref 49)	$2.7 \cdot 10^5$	(Ref 52)
T_L	K	2131	(Ref 53)	1727	(Ref 50)
T_S	K	2031		1627	
α_l	$-$	0.33	(Ref 54)	0.28	(Ref 55)
γ	$N\,m^{-1}$	$1.7 - 0.00032(T - T_{L_{Cr}})$	(Ref 49)	$1.943 - 0.00043(T - T_{L_{316L}})$	(Ref 56)
μ	$Pa\,s$	$\mu_{Cr}(T)$	(Ref 57)	0.005	(Ref 50)
μ_S	$Pa\,s$	100		100	
ρ_L	$kg\,m^{-3}$	6280	(Ref 53)	6900	(Ref 50)
ρ_S	$kg\,m^{-3}$	6700	(Ref 53)	7320	(Ref 50)

Table 5. Maximum surface temperature and velocity magnitude, and calculated Reynolds number of the system.

	$T_{melt\,surface}^{max}$	$U_{melt\,surface}^{max}$	Re
Turbulent model	$2900\ K$	$2.2\ m/s$	1485
Laminar model	$3200\ K$	$3.7\ m/s$	2602

Table 6. Maximum turbulent diffusivities and ratios of turbulent to intrinsic diffusivities.

	Momentum	Thermal	Mass
Maximum turbulent diffusivity $(\mathrm{m}^2/\mathrm{s})$	$5 \cdot 10^{-6}$	$4 \cdot 10^{-6}$	$6 \cdot 10^{-6}$
Maximum ratio of turbulent to intrinsic diffusivities	20	0.6	7000

8. Figures

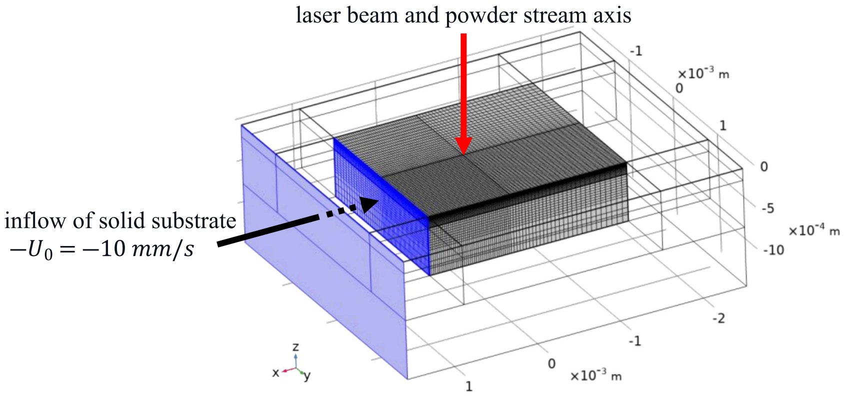

Figure 1. Geometry outlines of the entire domain, with a dense mesh in the fluid domain.

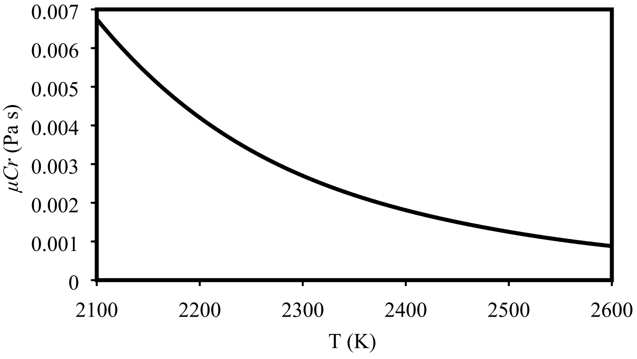

Figure 2. Evolution with temperature of the chromium viscosity μ_{Cr}.

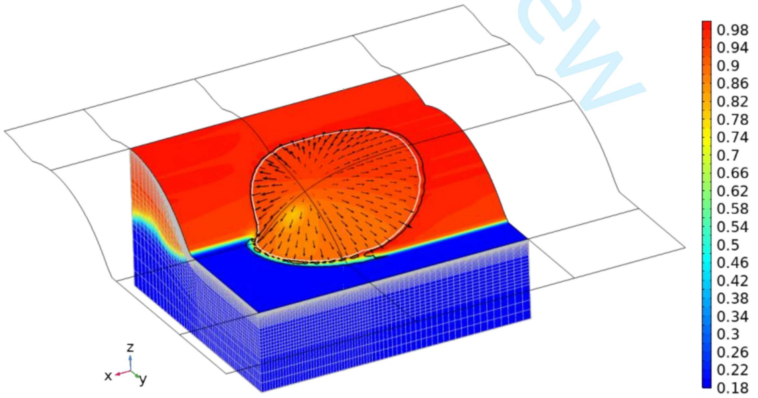

Figure 3. Turbulent model result with deformed top surface edges, Cr mass fraction color mapping in the fluid domain and velocity vectors at the melt pool surface (maximum arrow magnitude ~ 1.1 m/s). The black and white contours denote the solidification isotherms.

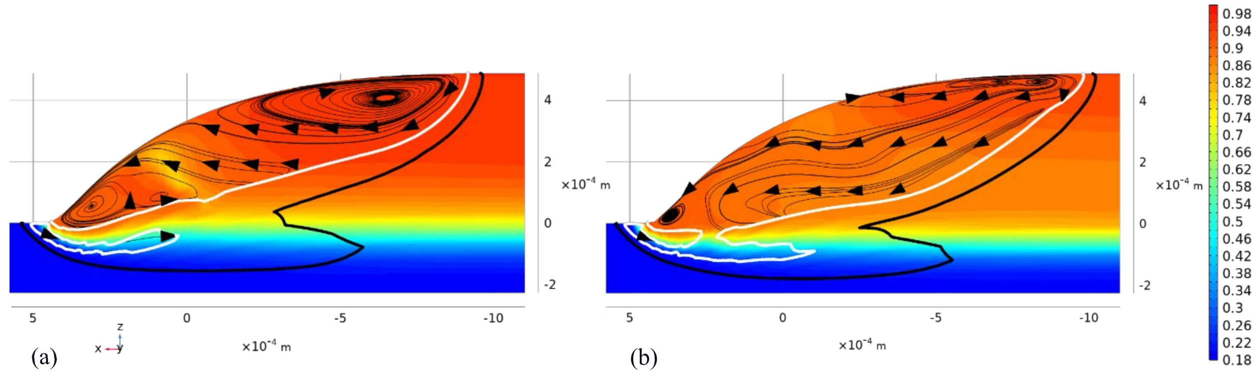

Figure 4. (a) Turbulent and (b) laminar model results, cross-length (xz cut plane at $y = 0$) with Cr mass fraction color mapping and 2D streamlines of the flow. Solidus and liquidus isotherms are represented as black and white lines respectively.

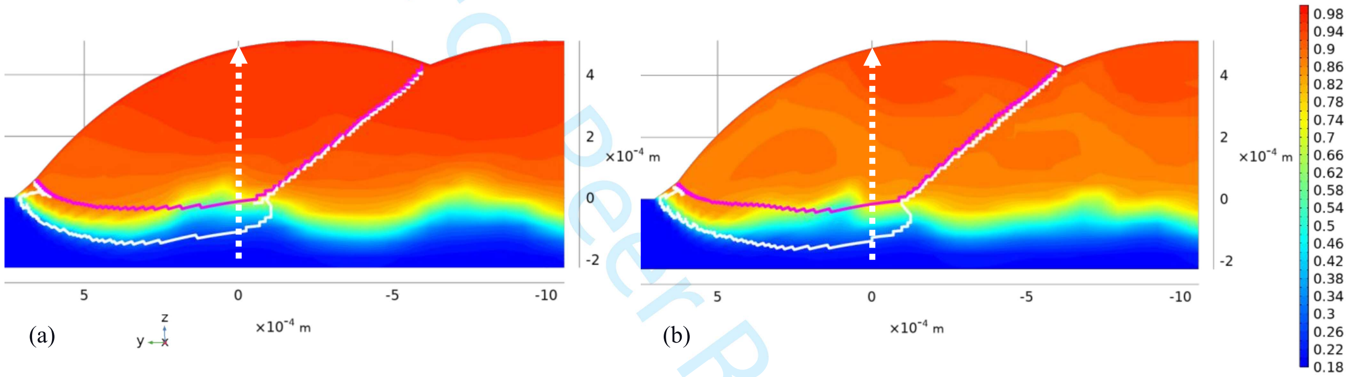

Figure 5. (a) Turbulent and (b) laminar model results, cross-section (yz cut plane at $x = -1\ mm$) after solidification of the Cr mass fraction color mapping with the contours of the molten zone, chromium liquidus (in magenta) and local liquidus (in white), projected along x. White dashed arrow: see figure 10.

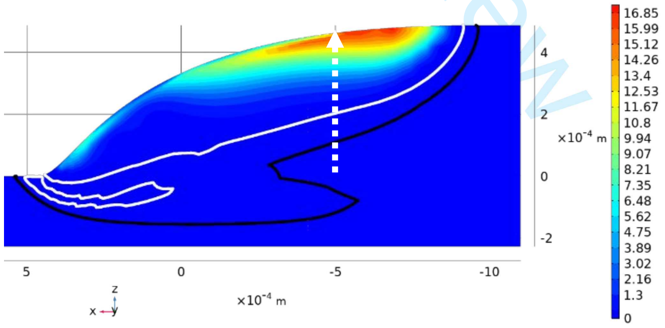

Figure 6. Turbulent model result, cross-length (xz cut plane at $y = 0$) color mapping of the ratio of turbulent viscosity to intrinsic viscosity with the solidus and liquidus isotherms. White dashed arrow: see figure 7.

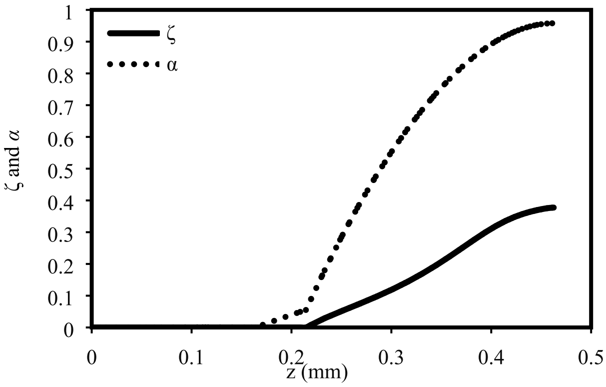

Figure 7. Turbulent model result, evolution of ζ and α along the dashed arrow displayed on figure 6.

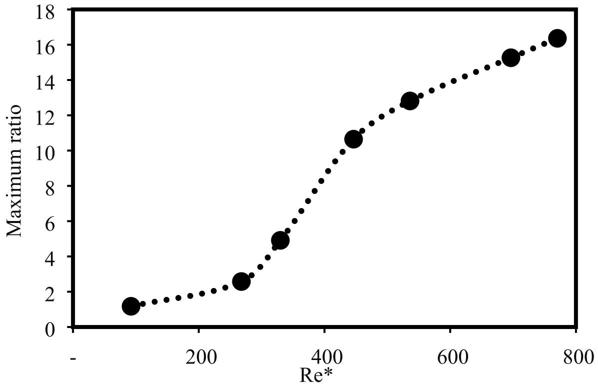

Figure 8. Turbulent model results, evolution of the ratio of turbulent viscosity ν_T on maximum intrinsic viscosity ν_0, for different Re* numbers.

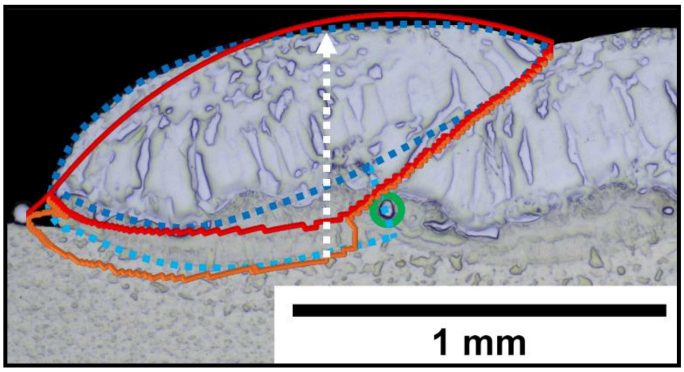

Figure 9. Microscopic image of the cross-section of the last track of the first Cr layer, with dashed blue contours encircling the melted area and the turbulent simulation result superimposed as red and orange contours. An undissolved Cr particle at the boundary between the chromium layer and 316L substrate is enclosed by a green circle. Dashed arrow: see figure 10.

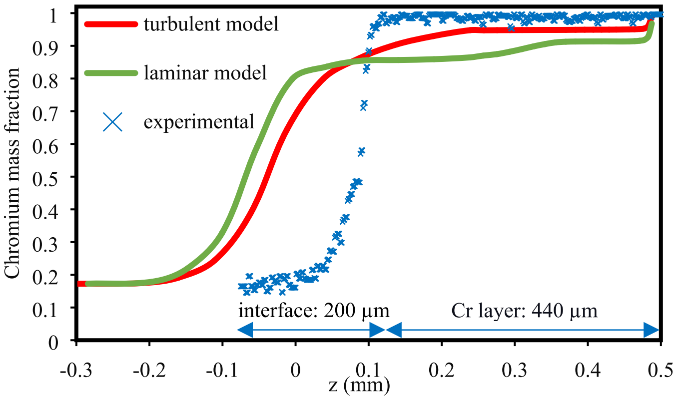

Figure 10. Vertical chromium mass fraction evolution along the dashed arrow displayed on figure 5 and comparison with the EDX profile distribution performed along the dashed arrow in figure 9. At the bottom is indicated the lengths of the chromium layer and of the boundary between the chromium layer and 316L substrate.